Reconstruction of Porous Media Using an Information Variational Auto-Encoder

Ting Zhang[1] · Hongyan Tu[1] · Pengfei Xia[1] · Yi Du[2]

© The Author(s), under exclusive licence to Springer Nature B.V. 2022

Abstract

The reconstruction of porous media is significant to some fields such as the study of seepage mechanics and reservoir engineering. Traditional methods have challenges in reconstruction quality due to their insufficient learning ability and suffer from lengthy computational time in large-quantity reconstruction tasks since they cannot reuse the parameters or models established previously. As a branch of deep learning, the variational auto-encoder (VAE) has shown excellent performance in extracting characteristics reflecting the underlying data manifold through a set of possible variables based on a latent model. Fisher information can help to balance the encoder and decoder in information control, used to estimate the variance of maximum likelihood estimate equation. Therefore, this paper proposes a method to reconstruct porous media based on VAE and Fisher information. Firstly, the structural characteristics of porous media are studied by the neural networks of the encoder to obtain the mean and variance of these characteristics. Then, the random sampling is carried out to reconstruct the intermediate results, and the optimization function of the encoder is combined with Fisher information to optimize the network. Finally, the intermediate results are input into the decoder to reconstruct porous media, and the optimization function of the decoder combined with Fisher information optimizes the reconstructed results. This method is evaluated by comparing the variogram, multiple-point connectivity, permeability and porosity of sandstone samples with some other typical reconstruction methods, showing its good reconstruction quality and efficiency.

Article Highlights

- **The reconstruction by our method is better than that of traditional methods.**
- **The proposed method can reuse the parameters or models established previously.**
- **The proposed method has a faster training speed.**

✉ Yi Du
  duyi0701@126.com

1 College of Computer Science and Technology, Shanghai University of Electric Power, Shanghai 200090, China

2 College of Engineering, Shanghai Polytechnic University, Shanghai 201209, China

1 Introduction

Understanding the internal structures of porous media is very important to reservoir engineering, environmental evaluation, seepage mechanisms, biomedicine and material science since microstructures in these scientific areas are required for further analyses of macroscopic properties. Since the internal structures of porous media are usually very complex, it is difficult to describe them with several specific parameters or functions. Researchers have done a lot of work on the 3D reconstruction of pore structures and developed reconstruction methods which are divided into two types: the experimental methods (Wirth 2004; Blunt et al. 2013) and numerical reconstruction methods (Okabe and Blunt 2005; Tahmasebi and Sahimi 2012; Karsanina et al. 2015).

The experimental methods include computed tomography (CT) scanning, focused-ion beam (FIB), transmission electron microscope (TEM), nuclear magnetic resonance (NMR), scanning electron microscope (SEM) (Arns 2004; Tomutsa et al. 2007; Wirth 2009; Stingaciu et al. 2010; Hemes et al. 2015), and so on. CT scanning uses the X-ray beams to penetrate porous media to directly obtain 3D images of pore spaces or detect other materials. Thanks to advances in CT technology, micro-CT and Nano-CT, respectively, can be used to obtain the images with micro-scale and nano-scale resolutions. The CT scanning is fast, clear and lossless, and its resolution is high in most cases, but it is expensive and inconvenient to prepare samples. For example, for some fragile rock samples like shale, it is not easy to make the sample for experiments. Other experimental methods usually suffer from the same problems like CT scanning.

Numerical reconstruction methods can be considered as good supplements for the experimental methods since they are relatively inexpensive and convenient by reusing real data previously obtained with physical devices. The earlier typical reconstruction methods were proposed only using the statistical information from 2D slices of porous media, e.g., the Gaussian field method using porosity and a two-point correlation function as constraints (Quiblier 1984; Ioannidis et al. 1995). To better describe the pore space, more information of structures was introduced, e.g., the simulated annealing algorithm whose objective function corresponds to the system energy (Hidajat et al. 2002), and the process-based simulation method simulating the formation process of sedimentary rocks (Bakke and Øren 1997; Øren and Bakke 2002).

The multiple-point statistics (MPS) is another important branch for the reconstruction of porous media since Okabe and Blunt (2004) used a typical MPS method called SNESIM (Strebelle 2002) to reconstruct porous media from only 2D slices of porous media. Based on the training images (TIs) reflecting the correlation in multiple points in the spatial structures, MPS extracts the patterns from TIs and then restores them to the final model. Two typical MPS methods are SNESIM (Strebelle 2002) and FILTERSIM (Zhang et al. 2006), which are two representatives for pixel-based MPS and pattern-based MPS. To overcome the memory limitations, as well as improve pattern reproduction quality, some other MPS methods were also developed, e.g., image quilting (Mahmud et al. 2014) introducing the stitching and splicing into the simulation, ISOMAP-based MPS (Zhang et al. 2016) using manifold learning for reconstruction and CCSIM (Tahmasebi et al. 2012) for the realizations of a reservoir with accurate conditioning and continuity.

Recently, deep learning has been widely used in many research fields related to feature extraction, and auto-encoder is one of the important technologies in deep learning. The auto-encoder is an unsupervised learning algorithm for learning the representation of the characteristics of input data. The concept of auto-encoder was first put forward by

Rumelhart et al. (1986). Hinton et al. (2006) derived a fast greedy algorithm (Cormen et al. 2009) based on the auto-encoder by using the "complementary prior" method, learned the deep network layer by layer, and then optimized the parameters of the whole network, thus producing the deep auto-encoder. Hinton's method is based on greedy strategy, that is, when solving the problem, always make the best choice in the current view. That is to say, instead of considering the global optimization, the algorithm obtains the local optimal solution. Bengio et al. (2006) added the constraint of sparseness to the learning process of deep auto-encoder and used as little neuron learning as possible to extract useful data features to generate sparse auto-encoder. Vincent et al. (2008) added noises to the input data to improve the robustness of the algorithm to form a denoising auto-encoder. Variational auto-encoder (VAE) model is a generative network based on variational Bayes (VB) inference proposed by Kingma and Welling (2014). A generative network can learn the distribution of input and generate corresponding output according to the properties of input information. Two common generative models in deep learning are VAE and generative adversarial network (GAN).

Compared with the traditional simulation or reconstruction methods, there are two important advantages introduced by deep learning and its branches. First, deep learning methods can reuse model parameters such as learning rates, training epochs, and weights. The second advantage relies on the strong ability of deep learning extracting characteristics from TIs, improving reconstruction quality.

Besides, thanks to the frameworks (e.g., Tensorflow and PyTorch) provided by the public deep learning communities, these deep learning methods can be used by common users even without knowing the complicated theories and design of parallelization for GPU. The detailed work about GPU is performed using the APIs of the frameworks like the black-box mechanism, which makes it easier for the general public.

VAE is a deep latent generation model and widely used in image generation. Latent variables are used in VAE. In statistics, latent variables, as opposed to observable variables, are variables that are not directly observed but are inferred through a mathematical model from other variables that are directly measured or observed. In VAE, a latent variable is the vector generated by the encoder according to the original input image, and then, an image can be reconstructed according to this latent variable.

VAE often suffers from its loss function, leading to the low-quality blurry images since the reconstruction tends to generate the mean of the generative distribution. Through continuous improvement to VAE's architectures and objective functions, many variants have been developed to address the above issue. Makhzani et al. (2015) proposed conditional variational auto-encoder (CVAE) to control VAE orientation to generate specific categories of sample data. The input of CVAE includes the training data and category labels, transferring VAE from an unsupervised mode to a semi-supervised mode. Louizos et al. (2015) proposed variational fair auto-encoder (VFAE) to separate the noise factor from the latent variable information and make the model learn the characteristic representation of some invariant factors more clearly. The importance weighted auto-encoder (IWAE) is another variant of VAE proposed by Burda et al. (2015) to improve the generalization ability of VAE. These above methods can generate different images according to different task requirements and greatly improve the quality of generated images.

In information theory, Fisher information has always been an important tool to describe information behavior in information systems. Fisher (1925) introduced Fisher information in the context of statistical estimation, which can describe the behavior of the dynamic system accurately (Vignat and Bercher 2003). In detail, Fisher information is a method

to measure the amount of information carried by observable random variable X about the unknown parameter θ of the distribution of model X. Formally, it is the variance score, or the expected value of observed information. Fisher information is used to estimate the variance of maximum likelihood estimate (MLE) equation. Its intuitive expression is that as more and more data are collected, the variance, which is in the form of independent sum, will become larger and larger, symbolizing more and more information to be obtained. Therefore, Fisher information is introduced to measure how much valuable information the sample data gives for the unknown parameters in the distribution.

Recent studies have reported that VAE is difficult to balance the information control between the encoder and the decoder in its structure (Samuel et al. 2015). For example, when the decoder is too expressive, latent variables generated by the encoder are almost ignored. Zheng et al. (2019) proposed Fisher auto-encoder (FAE) to balance Fisher information and Shannon information. Based on FAE, this paper applies Fisher information to the VAE approach for the 3D porous media reconstruction. The proposed method shows the advantage in terms of both quality and speed, verified by the reconstruction tests of sandstone.

2 Methodology

2.1 The Introduction of VAE

VAE is a kind of deep generative model based on VB generation networks. Two models of probability density distribution are established in VAE using two neural networks: One is the distribution of the encoder (i.e., $q_{\varphi}(z|x)$), used for the variational inference of original input data to generate the variational probability distribution of latent variables; the other is the distribution of the decoder (i.e., $P_{\theta}(x'|z)$) for reconstructing the data by generating the approximate probability distribution of the original data according to the variational probability distribution of the generated latent variables. The variational probability distribution is an approximate posterior probability distribution derived from the VB inference. The basic idea of VB is to transform the probability reasoning problem into a variational optimization problem through variational transformation. To simplify the calculation, VAE sets the variational distribution to a Gaussian distribution.

The typical structure of VAE is shown in Fig. 1 where "$+$" and "$*$", respectively, represent the addition and multiplication of elements; X is the input dataset and X' is the reconstructed result. X usually is high-dimensional and used as training data, whose underlying features are learned by the encoder. VAE uses stochastic gradient descent (SGD) to optimize the loss function which is the minimization of objective functions under constrained conditions. SGD randomly selects a group of data from the samples and updates them according to the gradient during the training process. Then re-select another group of data and update them again. Repeat this process until the convergence of the loss function is reached. To sum up, SGD is an effective optimization method that updates parameters until losses are within acceptable limits.

VAE needs to "re-parameterize" for optimization by introducing an auxiliary parameter ε which is obtained by sampling from the standard normal distribution $N(0,1)$. The intermediate latent variable z can be expressed by Eq. (1) (Rezende and Mohamed 2015):

Fig. 1 A typical VAE network diagram

$$z = \mu + \sigma * \varepsilon \tag{1}$$
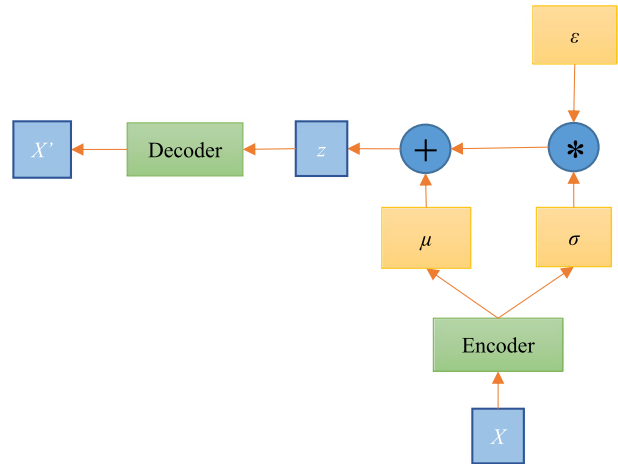
where σ and μ are, respectively, the standard deviation and mean of Gaussian distribution calculated from the encoder. The encoder distribution $q_\varphi(z|x)$ parameterized by a variational parameter φ (Kingma and Welling 2014) is introduced into the encoder network to replace the undetermined real posterior distribution $P_\theta(z|x)$. φ is approximately considered as the weights of the encoder, and θ is approximately considered as the weights of the decoder. The evidence lower bound (ELBO) function $L(\theta, \varphi; X)$ is defined as follows:

$$L(\theta, \varphi; X) = \underbrace{E_{q_\varphi(z|x)} \log_2(P_\theta(x'|z))}_{\text{reconstruction error}} - D_{KL}(q_\varphi(z|x)|P_\theta(z)) \tag{2}$$

where D_{KL} represents the KL divergence; $P_\theta(x'|z)$ is a θ-parameterized decoder distribution; $P_\theta(z)$ represents the probability distribution of the latent variable z. Kullback–Leibler (KL) divergence is used to measure the difference between $q_\varphi(z|x)$ and $P_\theta(z)$, which can be computed explicitly. Finally, z is input into the decoder model $P_\theta(x'|z)$ to obtain the final reconstruction X'. It seems $L(\theta, \varphi; X)$ has a penalty item (i.e., KL divergence) and a reconstruction error. To maximize $L(\theta, \varphi; X)$ (i.e., ELBO), the constraint parameters φ and θ are repeatedly trained and optimized to minimize the KL divergence and maximize the reconstruction error according to Eq. (2) (Kingma and Welling 2014; Nash and Williams 2017).

2.2 Fisher Information and Shannon Entropy

As mentioned above, maximizing ELBO needs to maximize the reconstruction error and minimize the KL divergence, but maximization of the reconstruction error and minimization of the KL divergence are contradictory. Therefore, it is necessary to balance between the reconstruction error and the KL divergence (Samuel et al. 2015; Chen et al. 2016; Zhao et al. 2017). As can be seen from $L(\theta, \varphi; X)$ in Eq. (2), only the KL divergence is considered as a penalty item for regularization. Since the representation of the VAE encoder is controlled by the divergence but there is no control exerted on the VAE decoder, some schemas based on information theory were used to solve this problem (Chen et al. 2016;

Zhao et al. 2017; Zheng et al. 2019), e.g., a constraint item based on Shannon entropy is introduced in ELBO to ensure that latent variables can learn sufficient data characteristics since Shannon entropy can prevent the approximate inference distribution from being significantly different from the true posterior, thus improving the quality of representation learning (Zheng et al. 2019). However, Shannon information is usually difficult to be processed in calculation, and only approximate substitutes can be obtained in previous studies.

For a continuous probability distribution function (PDF), Shannon entropy (Shannon and Weaver 1949) is a measure of global distributions, which is less sensitive to changes in distribution occurring over a small area. Fisher information is quite different from Shannon entropy (Fisher 1922; Frieden 2004). The former is a measure of the gradient content of the distribution, so it is quite sensitive to small local disturbances (Rosso et al. 2015). Let the Shannon entropy and Fisher information of input images X be $H(X)$ and $J(X)$, respectively. Fisher information is defined as follows:

$$J(X) = \int_x \left(\frac{\partial}{\partial x} f(x) \right)^2 \frac{dx}{f(x)} \tag{3}$$

Shannon entropy is usually converted into the form of entropy weight (Vignat and Bercher 2003):

$$N(X) = \frac{\exp(2H(X))}{2\pi \exp(1)} \tag{4}$$

where exp represents the exponential function with the base e. When X represents a random vector and Fisher information $J(X)$ represents a Fisher information matrix, the relation between $N(X)$ and the trace of $J(X)$ is (Dembo et al. 1991; Vignat and Bercher 2003):

$$N(X) \cdot tr(J(X)) = K , \; K \geq 1 \tag{5}$$

where K is a constant and $tr(\cdot)$ represents the trace of the matrix. As shown in Eq. (5), Fisher information and Shannon entropy are intrinsically related (Schrödinger 1930) and have the nature of uncertainty, in which the higher Fisher's information is, the lower Shannon entropy is (Dembo et al. 1991), but the calculation of Fisher information is usually easier than Shannon entropy. Hence, Fisher information is considered to be complementary for Shannon entropy and used in this paper.

2.3 The Information Variational Auto-Encoder

Fisher information is used to balance the encoder and decoder of the VAE model (Zheng et al. 2019). According to Eq. (5), it can be found that there is a relationship between Fisher information $J(X)$ and Shannon entropy weight $N(X)$. Shannon entropy is usually difficult to be processed in calculation (Phuong et al. 2018), so Fisher information instead of Shannon entropy is used to calculate information and two new penalty items are proposed for it. The proposed method is called information variational auto-encoder (IVAE) hereafter, which not only includes the KL divergence as a penalty item, but also includes Fisher information as two penalty items in the encoding stage and decoding stage, respectively, i.e., IVAE maximizes $L(\theta, \varphi; X)$ under the constraint of Fisher information. The $L(\theta, \varphi; X)$ of IVAE is:

$$L(\theta, \varphi; X) = \underbrace{E_{q_\varphi(z|x)} \log_2 P_\theta(x'|z)}_{\text{reconstruction error}} - D_{KL}(q_\varphi(z|x)|P_\theta(z)) \underbrace{- \lambda_z |tr(J(z)) - F_z|}_{PI-1} \underbrace{- \lambda_{x'} |tr(J(x')) - F_{x'}|}_{PI-2}$$

(6)

Compared with $L(\theta, \varphi; X)$ shown in Eqs. (2), (6) adds two more penalty items (PI-1 and PI-2) that adjust the encoder and decoder, respectively: PI-1 controls Fisher information of the encoder network and PI-2 controls Fisher information of the decoder network. λ_z and $\lambda_{x'}$ are adjustment coefficients. Both $F_{x'}$ and F_z are positive constants, representing the expected Fisher information values in the decoder and the encoder, respectively, meaning that Fisher information in the decoder and encoder can be controlled by $F_{x'}$ and F_z. The larger $F_{x'}$ and F_z are, the more likely the distribution is estimated by the θ- and φ-parameterized model; otherwise, the smaller $F_{x'}$ and F_z show that the influence of Shannon entropy is enhanced. Fisher information estimation can be directly calculated according to its definition (Stam 1959).

The optimization procedures of the model are discussed, respectively, for the encoder network and decoder network in the following section. Take the encoder network as an example. If the Fisher information is only considered in the encoder network, set $\lambda_{x'} = 0$ in Eq. (6). The ELBO of the encoder network, denoted as $L_e(\theta, \varphi; X)$, contains the divergence item and information error item:

$$L_e(\theta, \varphi; X) = -D_{KL}(q_\varphi(z|x)|P_\theta(z)) - \lambda_z |tr(J(z)) - F_z|$$

(7)

Compared with Eqs. (6), (7) lacks a reconstruction error. The posterior distribution $q_\varphi(z|x)$ is a normal distribution, and $P_\theta(z)$ is a standard normal distribution. Therefore, the KL divergence in Eq. (7) is calculated as (Kingma and Welling 2014):

$$D_{KL}(q_\varphi(z|x)|P_\theta(z)) = -\frac{1}{2}((1 + \log_2(\sigma)^2) - (\mu)^2 - (\sigma)^2)$$

(8)

According to the definition, the Fisher information in Eq. (7) can be obtained (James 2011):

$$tr(J(z)) = \int_z \left(\frac{\partial}{\partial z} q_\varphi(z|x) \right)^2 dz = \frac{1}{\sigma^2}$$

(9)

Equations (8) and (9) are substituted in Eq. (7), and then $L_e(\theta, \varphi; X)$ is:

$$L_e(\theta, \varphi; X) = \frac{1}{2}((1 + \log_2(\sigma)^2) - (\mu)^2 - (\sigma)^2) - \lambda_z |\frac{1}{\sigma^2} - F_z|$$

(10)

Similarly, Fisher information is used with ELBO at the decoder, denoted as $L_d(\theta, \varphi; X)$. Then set $\lambda_z = 0$ in Eq. (6), and $L_d(\theta, \varphi; X)$ is:

$$L_d(\theta, \varphi; X) = \underbrace{E_{q_\varphi(z|x)} \log_2 P_\theta(x'|z)}_{\text{reconstruction error}} - \lambda_{x'} |tr(J(x')) - F_{x'}|$$

(11)

As shown in Eq. (2), the original VAE only considers KL divergence and a reconstruction error, while IVAE includes a reconstruction error and three penalty items (KL divergence, PI-1 and PI-2) related to Fisher information and KL divergence, as shown in Eq. (6). IVAE balances both the likelihood estimation and the dependence between input data and latent

variables through the new penalty items, making the new model consider KL divergence and Fisher information together to improve reconstruction quality.

2.4 Architecture and Parameters Description

The architecture and parameters description are shown in Tables 1, 2 and 3.

3 Procedures of the Proposed Method

The steps of the proposed method are as follows:

Step 1. Input the TIs of porous media. Design the network architecture and initialize all parameters.

Step 2. Use the SGD to update the parameters and set the learning rate.

Step 3. Use the deep neural network to iteratively fit the training data. The probability distribution and information content of the training data are obtained. Optimize the encoder network according to Eq. (7).

Table 1 Parameter description in network architecture and operations

Conv3D	Filters: The dimensionality of the output space. kernel_size: Height and width of the 3D convolution window. strides: The moving distance of the convolution along each spatial dimension. padding: The filling method.activation: Activation function
LeakyReLU	Alpha (α): Negative slope coefficient
Upsampling3D	Size: The upsampling factors
BatchNormalization	Momentum: An attenuation rate
Dense	Units: Dimensionality of the output space

Table 2 The network architecture of the encoder

Layers	Structure	Parameters
Layer1	Conv3D LeakyReLU BatchNormalization	FILTERS = 64, Kernel_size = 4, Strides = 2, Padding = same Alpha = 0.2 Momentum = 0.8
Layer2	Conv3D LeakyReLU BatchNormalization	Filters = 128, Kernel_size = 4, Strides = 2, Padding = same Alpha = 0.2 Momentum = 0.8
Layer3	Conv3D LeakyReLU BatchNormalization	Filters = 256, Kernel_size = 4, Strides = 2, Padding = same Alpha = 0.2 Momentum = 0.8
Layer4	Conv3D LeakyReLU BatchNormalization	Filters = 512, Kernel_size = 4, Strides = 2, Padding = same Alpha = 0.2 Momentum = 0.8
Layer5	Conv3D LeakyReLU BatchNormalization	Filters = 1024, Kernel_size = 4, Strides = 2, Padding = same Alpha = 0.2 Momentum = 0.8
Layer6	Dense	Units = 256

Table 3 The network architecture of the decoder

Layers	Structure	Parameters
Layer1	Dense	Units = 256
Layer2	Upsampling3D Conv3D BatchNormalization	Strides = 2 Filters = 512, Kernel_size = 4, Strides = 1, Padding = same, Activation = relu Momentum = 0.8
Layer3	Upsampling3D Conv3D BatchNormalization	Strides = 2 Filters = 256, Kernel_size = 4, Strides = 1, Padding = same, Activation = relu Momentum = 0.8
Laye4	Upsampling3D Conv3D BatchNormalization	Strides = 2 Filters = 128, Kernel_size = 4, Strides = 1, Padding = same, Activation = relu Momentum = 0.8
Layer5	Upsampling3D Conv3D BatchNormalization	Strides = 2 Filters = 64, Kernel_size = 4, Strides = 1, Padding = same, Activation = relu Momentum = 0.8
Layer6	Upsampling3D Conv3D	Strides = 2 Filters = 1, Kernel_size = 4, Strides = 1, Padding = same, Activation = sigmoid

Step 4. The random sampling results from $N(0, 1)$ as well as σ and μ obtained from the encoder network are substituted in Eq. (1) to calculate the intermediate latent result z. Once the training loss reaches the threshold of the loss function, the network parameters of the encoder are saved.

Step 5. Take the intermediate latent result z as the input of decoder network. The decoder network is iteratively optimized according to Eq. (11), and z is decoded. The final decoding result from decoder is the final reconstruction result, and the network parameters of the decoder are saved.

The flowchart of the above procedures is shown in Fig. 2. The output of VAE is subject to the latent variables imposed by an explicit distribution. The distribution of input data encoded into the latent variable space is optimized iteratively to approach the standard Gaussian distribution. In this paper, the IVAE model is applied to the reconstruction of porous media, and the Fisher information is taken as the penalty items, respectively, in the encoder and decoder. According to the characteristics extracted from the TI, the reconstruction of porous media can be realized.

4 Experimental Results and Analyses

In this section, a range of experiments, performed with an Intel Core i5 (3.5 GHz) CPU, 8 GB memory and GeForce GTX970 GPU (4 GB video memory), were conducted to evaluate the reconstruction quality and applicability of IVAE in the reconstruction of porous media. The experimental software framework for IVAE is TensorFlow-GPU.

4.1 Training Data and Representative Elementary Volume

The experimental sample is a cylindrical sandstone with a diameter of 3 mm. The 3D spatial data of the sample were obtained by scanning the real sandstone sample with synchrotron radiation X-rays, and the resolution is 10 microns per voxel. Figure 3 shows three
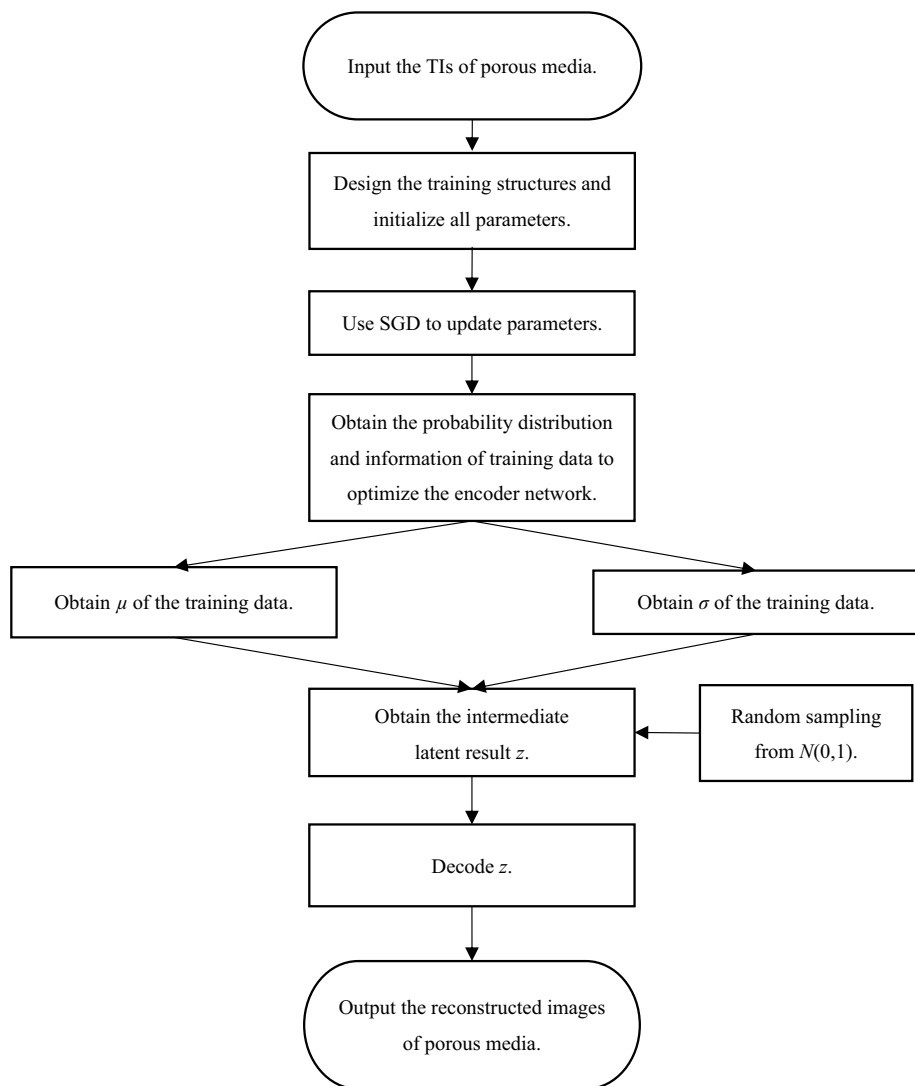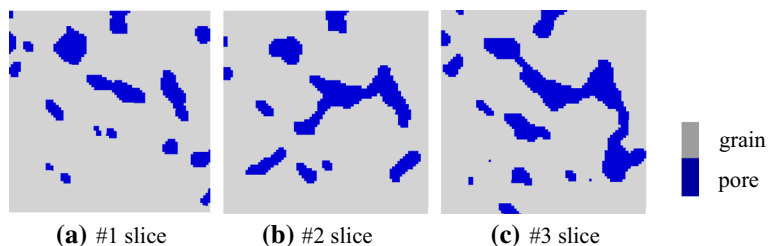
Fig. 2 The flowchart of the proposed method

(a) #1 slice   **(b)** #2 slice   **(c)** #3 slice

Fig. 3 Three slices of sandstone from synchrotron radiation X-rays scanning

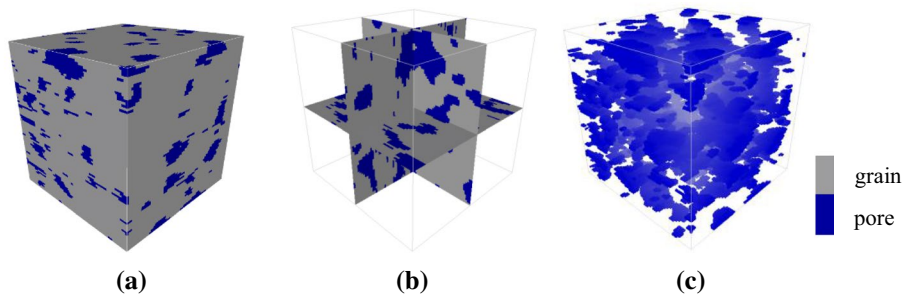**Fig. 4** The TI of sandstone. **a** Surface; **b** slices (X=40, Y=40, Z=40); **c** pore space

slices of the sandstone images with two facies: grain (gray) and pore (blue). 80 squares with 80×80 pixels each were continuously taken from 80 scanned images, stacked in sequence to form a TI of sandstone with $80\times80\times80$ voxels (porosity=0.1705). The surface, slices (X=40, Y=40, Z=40) and pore space of the TI are shown in Fig. 4.

Before implementing any reconstruction tests, representative elementary volume (REV) of the training data should first be determined (Oda 1988). It is important to observe the effect of sample size on the reconstruction of porous media. RVE refers to the minimum volume with basically stable properties of the sample under study, within which the characteristics of the sample tend to be stable. When the size or volume of the sample is smaller than an REV, the performance of the sample is likely to change with different sizes, and the characteristics of the sample possibly fluctuate significantly (Costanza et al. 2011).

There are two main ways to identify REV. One is widely used in soil science and hydrology based on porosity without considering macroscopic parameters. The other is based on some macroscopic parameters rather than microscopic ones and is commonly used in engineering mechanics (Nordahl and Ringrose 2008; Al-raoush and Apostolos, 2010).

For heterogeneous porous media, when the size of porous media is not large enough, the porosity tends to change greatly. Therefore, variogram $\gamma(h)$ instead of porosity is used to determine an REV in this paper. $\gamma(h)$ is usually used to reflect the correlation and variability of spatial structures, formulated in Eq. (12):

$$\gamma(h) = \frac{1}{2}E\{[Z(x+h) - Z(x)]^2\} \tag{12}$$

where E means the mathematical expectation; $Z(x)$ is an attribute value at the location x; h is the lag distance between two locations x and $x+h$.

The specific procedure to determine an REV used in our experiments is: first draw the variogram curves of the studied sample in the X, Y and Z directions; when the curve of a direction tends to be stable, the corresponding length along this direction is recorded as a side length of the REV. Repeat this procedure for all the variogram curves in the X, Y and Z directions, the REV can be obtained with its three side lengths determined by the location where variograms begin to become stable or flat. As long as the sample size is larger than an REV, this sample can be used as test data.

The variogram curves in the X, Y and Z directions of sandstone are calculated, respectively, as shown in Fig. 5. The abscissa represents h (unit: voxel), and the ordinate represents $\gamma(h)$. The variograms of the three directions tend to be stable at $h=12$, 15 and 12 (shown in red dotted lines), so the REV is considered as a $12\times15\times12$ cuboid, meaning that the TI is larger than the REV and can be used for our experiments.
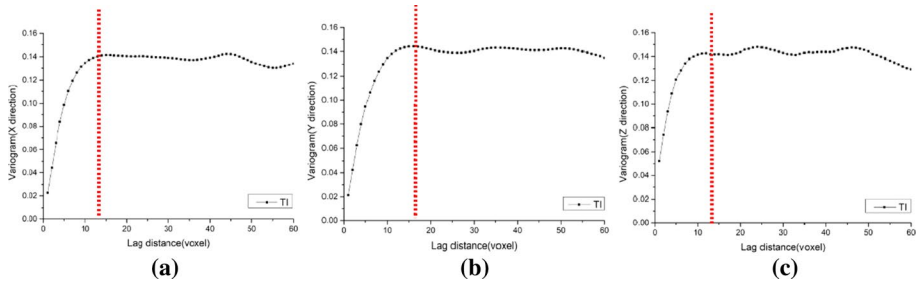
Fig. 5 Variograms of sandstone in three directions. **a** X direction; **b** Y direction; **c** Z direction

4.2 Reconstructions and Comparisons

4.2.1 Comparison of the TI and Reconstructed Images

In the section, IVAE, VAE, and two typical MPS methods SNESIM and direct sampling (DS) were, respectively, used to reconstruct porous media for comparison. The main parameters of IVAE are initialized as follows: The learning rate is 0.01; the number of training epochs is 4000; $\lambda_z = \lambda_{x'} = 0.1$; $F_{x'} = F_z = 5$. The threshold of training loss is 0.0001. As mentioned above, a cube with $80 \times 80 \times 80$ voxels is used as the TI, which is then divided into $4 \times 4 \times 4$ cubic non-overlapping subsamples with $20 \times 20 \times 20$ voxels each. Now there are altogether 64 non-overlapping 20-cubed subsamples used as the training dataset for IVAE and VAE. As for SNESIM and DS, the TI ($80 \times 80 \times 80$ voxels) is not necessarily separated and therefore used as a whole.

Figures 6, 7, 8 and 9 are the reconstructed images ($80 \times 80 \times 80$ voxels) using IVAE, VAE, SNESIM and DS. It can be found that the results of the four reconstruction methods all have similar long-connected pore spaces with the TI, but the porosity of the IVAE-reconstructed one is closest to that of the TI, as shown in Table 4, in which the bold number means it is best in the metrics.

For two binary numbers (i.e., 0 or 1), define an XOR operation: if the two numbers are same, the XOR result is 0; otherwise, it is 1. Assume when a voxel is pore, its corresponding state is 1; otherwise, the voxel state is 0. XOR operation can be used to judge the similarity between the generated data and the training data. After the XOR operation between the reconstruction and the TI, the percentage of voxels with a XOR result of 1 is used as
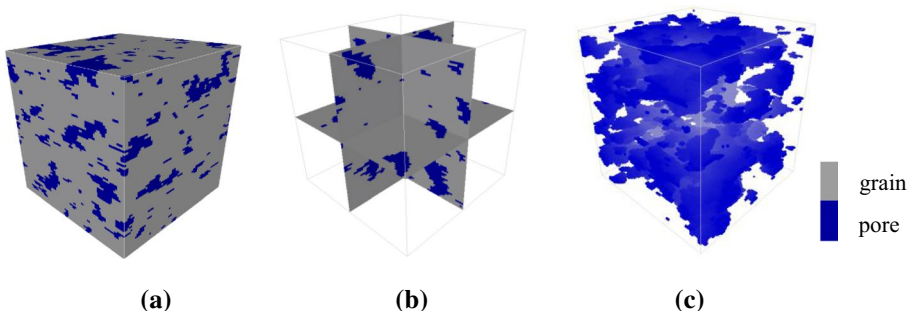

Fig. 6 A reconstructed image using IVAE. **a** surface. **b** slices (X = 40, Y = 40, Z = 40). (**c**) pore space
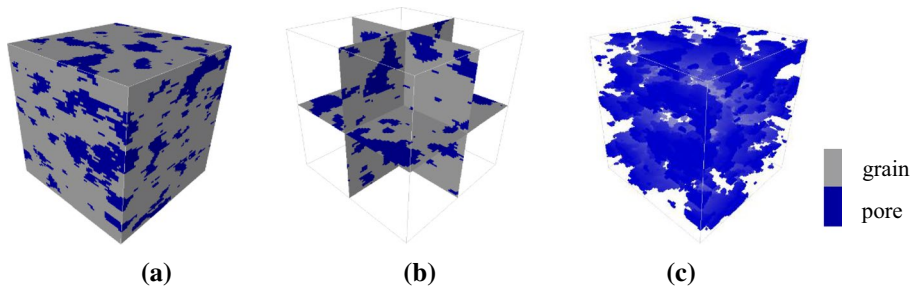
Fig. 7 A reconstructed image using VAE. **a** surface; **b** slices (X=40, Y=40, Z=40); **c** pore space
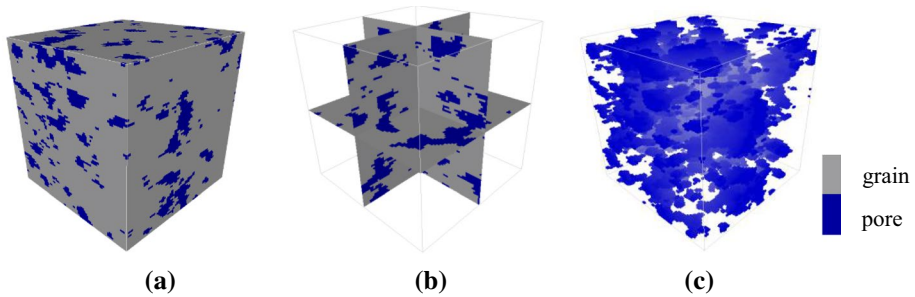

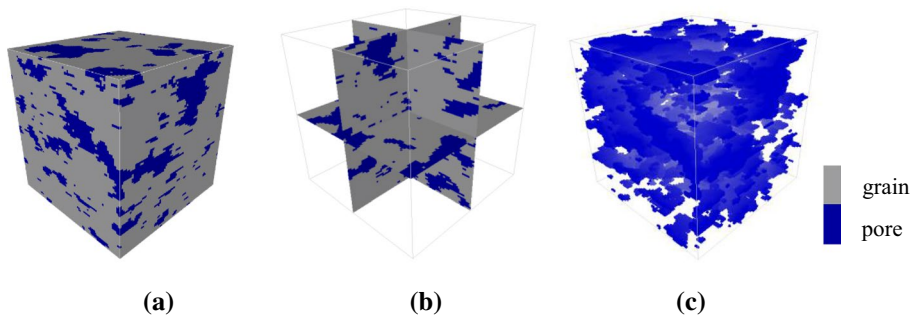**Fig. 8** A reconstructed image using SNESIM. **a** surface; **b** slices (X=40, Y=40, Z=40); **c** pore space

Fig. 9 A reconstructed image using DS. **a** surface; **b** slices (X=40, Y=40, Z=40); **c** pore space

		TI	SNESIM	VAE	DS	IVAE
Table 4 Porosities of the TI and the reconstructed images of IVAE, SNESIM, VAE and DS.	Porosity	0.1705	0.1805	0.1624	0.2105	**0.1765**

the similarity degree. When the percentage is close to 1, it means that the similarity degree between the TI and the reconstructions is very low. When the percentage is close to 0, it means overfitting. The similarity degree of IVAE-reconstructed result is 26.2%, which is a relatively reasonable index.

Reconstruction	SNESIM	VAE	DS	IVAE
#1	0.1805	0.1657	0.2105	0.1765
#2	0.1809	0.1683	0.2093	0.1715
#3	0.1736	0.1725	0.1976	0.1648
#4	0.1777	0.1558	0.1874	0.1707
#5	0.1873	0.1789	0.1987	0.1785
#6	0.1877	0.1526	0.1775	0.1750
#7	0.1766	0.1714	0.2045	0.1775
#8	0.1773	0.1563	0.1858	0.1717
#9	0.1174	0.1607	0.1772	0.1646
#10	0.1851	0.1698	0.2113	0.1712
Average of 10 porosities	0.1744	0.1652	0.1960	**0.1722**
Variance of 10 porosities	0.00042	0.00007	0.00018	**0.00002**

To obtain an average performance in porosity, IVAE, VAE, SNESIM and DS were used to reconstruct the sandstone sample ($80 \times 80 \times 80$ voxels) for another 10 times. As shown in Table 5, the porosity of 3D images reconstructed by IVAE is closer to that of the TI (porosity = 0.1705), and the variance is the smallest, indicating high reconstruction quality and low fluctuation.

4.2.2 Comparison of Variograms

Variograms not only can be used in the determination of an REV, but also can be used to evaluate the reconstruction quality. In this section, the variogram curves of the TI and IVAE-, VAE-, SNESIM- and DS-reconstructed images were calculated in the three directions of X, Y and Z, respectively, as shown in Fig. 10. In general, the variogram curve of IVAE is closer to that of the TI, especially in the Z direction.

Since variograms cannot provide a quantitative measure for the difference degree (*DD*) between the TI and the reconstructed results, a *DD* is defined between the TI and reconstructions using variograms:

$$DD(TI, re) = \sum_{h=1}^{n} \left(X_h - x_h \right)^2 \tag{13}$$

where *re* represents the method for reconstruction; X_h and x_h are variogram values of the TI and the reconstructed results with the distance *h*. A smaller *DD* means a lower difference degree. The *DD*s between the TI and reconstructions measured by variograms are shown in Table 6, calculated based on Fig. 10. The *DD*s between the TI and the reconstructions using IVAE are smallest in the X, Y and Z directions.

4.2.3 Comparison of Multiple-Point Connectivity

Variograms can only reflect the spatial continuity of two points in space. To evaluate the joint variability or connectivity of multiple points simultaneously, multiple-point connectivity (MPC) (Strebelle 2002) is used as a supplement for variograms, which is defined as:
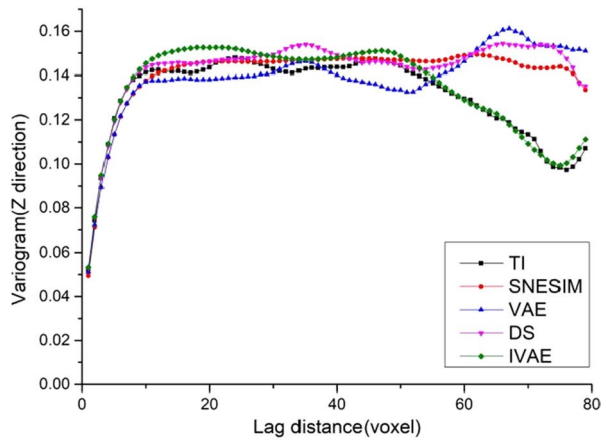
Fig. 10 Variograms of the TI and reconstructed images using SNESIM, IVAE, VAE and DS in three directions
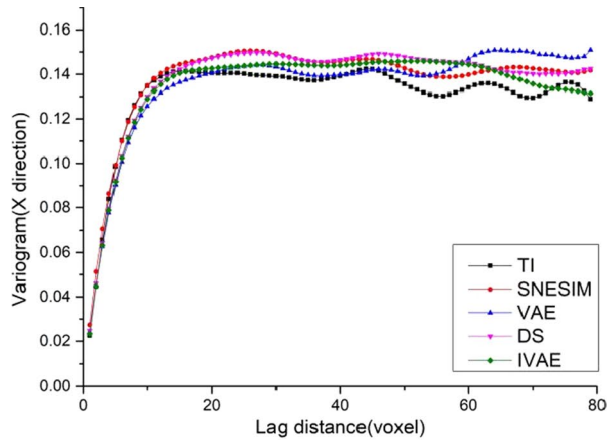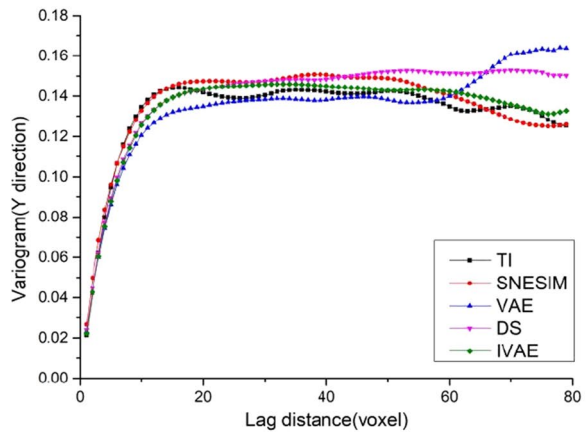
(a) X direction

(b) Y direction

(c) Z direction

Table 6 Difference degrees between the TI and reconstructions measured by variograms

Directions	Difference degrees (*DD*s)			
	DD(TI, SNESIM)	*DD*(TI, DS)	*DD*(TI, VAE)	*DD*(TI, IVAE)
X	0.1376	0.1701	0.0332	**0.0079**
Y	0.1201	0.2213	0.0629	**0.0312**
Z	0.2205	0.2458	0.1041	**0.0879**

$$MPC(n) = E\{S(u) \cdot S(u+1) \cdots \cdots S(u+(n-1) \cdot h)\} = E\left\{ \prod_{i=0}^{n-1} S(u+i \cdot h) \right\} \quad (14)$$

where $S(u)$ represents the attribute value at the position u; h is the lag distance; n is the number of voxels or pixels in one direction; E is the mathematical expectation. For porous media in this paper, $S(u)=1$ when u corresponds to pore space; otherwise, $S(u)=0$. As shown in Fig. 11, the MPC curve of IVAE is most similar to those of the TI.

Similar to the way of measuring the variogram curves in Fig. 10, the *DD*s between the TI and reconstructions measured by MPC curves are shown in Table 7, calculated based on Fig. 11. The *DD*s between the TI and the IVAE-reconstructed image are smallest.

4.2.4 Comparison of Permeability

Permeability is related to porosity, geometry of pores and other factors and displays the ability of fluids passing through porous media. In this section, the Lattice Boltzmann Method (LBM) (Okabe and Blunt 2004; Zhang et al. 2016) is used to calculate the permeability of porous media. A 3D 19-velocity model of LBM, called D3Q19, was used to compute the permeabilities of reconstructed images. There are altogether 19 velocity vectors defined in this model. The conditions of no-slip velocity are reached by the bounce-back scheme. Since the reconstructed results are cubic in our experiments, two parallel faces are open and the other four are sealed when supposing the fluids are perpendicularly passing through the two open parallel faces. Hence, there are altogether three directions for the computation of permeabilities using the Darcy's law. The detailed procedures and equations can refer to Zhang et al. (2016) or Okabe and Blunt (2004).

The data of the TI and the reconstructed images were, respectively, used as the input files of LBM simulation to calculate the permeabilities of those 3D images with the size of $80 \times 80 \times 80$ voxels. As shown in Table 8, the permeability of the TI and the average permeabilities of ten reconstructed images using IVAE, VAE, SNESIM and DS in three directions were computed by LBM. The permeabilities of IVAE are most similar to those of the TI.

4.2.5 Distribution and Numbers of Pores

Analyses of pore structures were, respectively, performed by the software Avizo (2009) through importing the TI, the reconstructed images of SNESIM, VAE, DS and IVAE. The structures of the pores including the number of pores and the diameter of pores are calculated.

The diameter of a pore is defined as:

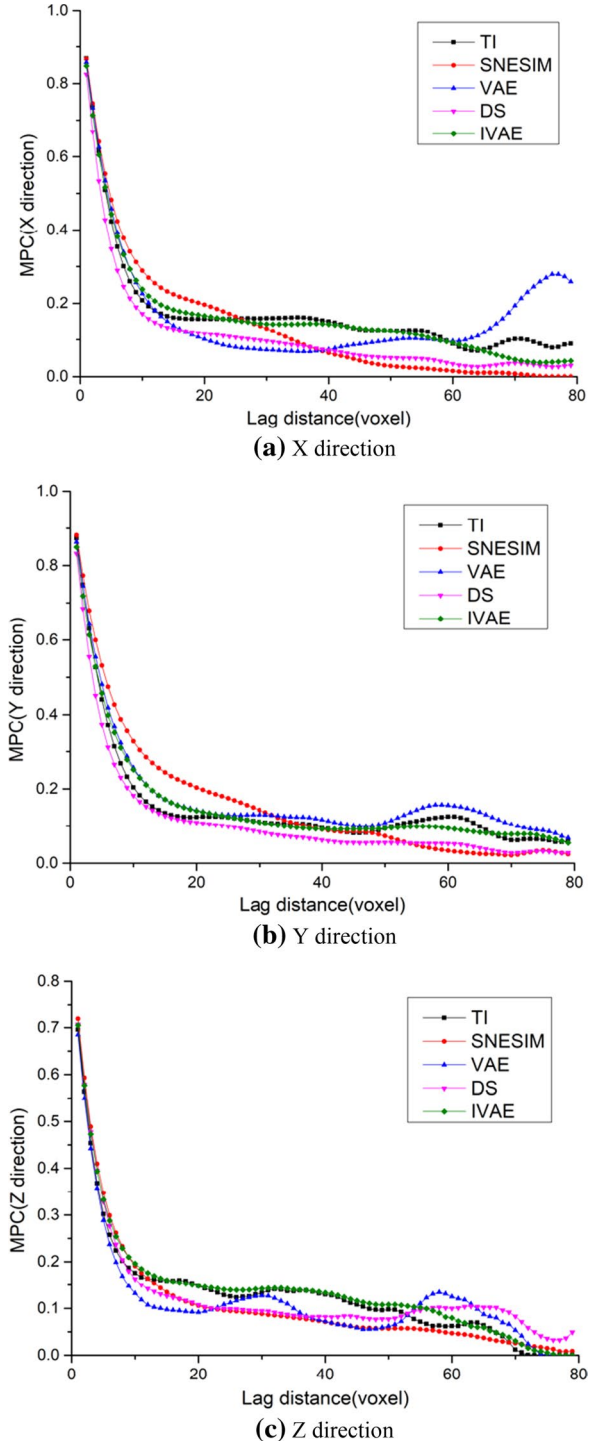**Fig. 11** MPC curves of the TI and reconstructed images using SNESIM, IVAE, VAE and DS in three directions

(a) X direction

(b) Y direction

(c) Z direction

Table 7 Difference degrees between the TI and reconstructions measured by MPC curves

Directions	Difference degrees (*DD*s)			
	DD(TI, SNESIM)	*DD*(TI, DS)	*DD*(TI, VAE)	*DD*(TI, IVAE)
X	0.1730	0.2983	0.2505	**0.0283**
Y	0.1932	0.1823	0.1380	**0.0096**
Z	0.1071	0.0746	0.0963	**0.0443**

Table 8 Average permeabilities of the TI and ten reconstructed images in three directions

Direction	Permeability (mD)				
	TI	SNESIM	IVAE	VAE	DS
X	1.637	1.472	**1.643**	1.869	1.531
Y	1.176	1.244	**1.217**	1.531	0.808
Z	1.375	1.004	**1.384**	1.325	1.037

Table 9 The average number of pores in the TI and 10 reconstructed images of each method

	TI	SNESIM	VAE	DS	IVAE
Number of pores	182	162	210	199	**189**

$$\text{diameter} = \sqrt[3]{\frac{6V}{\pi}} \tag{15}$$

where V is the volume of a pore. The number of pores in the TI and the average number of pores in the 10 reconstructed images by SNESIM, VAE, DS and IVAE are shown in Table 9. The maximum, minimum and average pore diameters in the TI and reconstructed images are shown in Table 10. It is seen that the pore number and pore diameters of IVAE are closer to those of the TI in general. In Fig. 12, the pore distribution of the TI is more similar to that of IVAE, indicating the better quality of IVAE.

4.2.6 The Influence of Different Network Layers

In this section, we will discuss the influence of different layer numbers of the encoder and the decoder on the reconstructed results. To facilitate the discussion, we set the same layer numbers for the encoder and the decoder in our experiment, meaning the layer numbers in the encoder and the decoder are same. Table 11, respectively, shows the reconstruction times for i (= 4, 6, 8, 10, respectively) layers, where i is the layer number of the encoder and the decoder of IVAE. It can be seen that with the increase of i, the reconstruction time also increases. Figure 13 shows the MPC curves in three directions. Normally more layers can improve reconstruction quality, but the corresponding reconstruction time also increases sharply, meaning that the reconstruction time and quality should be balanced in real simulation. Currently it seems that a 6-layer network of the encoder and the decoder is a proper balance for reconstruction quality and time in our experiments.

Table 10 Pore diameters in the TI and the reconstructed images of each method

Pore diameters	TI	SNESIM	VAE	DS	IVAE
Average diameter (voxel)	9.65	9.16	9.34	9.27	**9.48**
Maximum diameter (voxel)	23.74	21.32	20.15	21.17	**22.83**
Minimum diameter (voxel)	2.01	1.8	1.94	**2.11**	2.17

Fig. 12 The distribution of pore diameters of the TI and the reconstructed images of each method
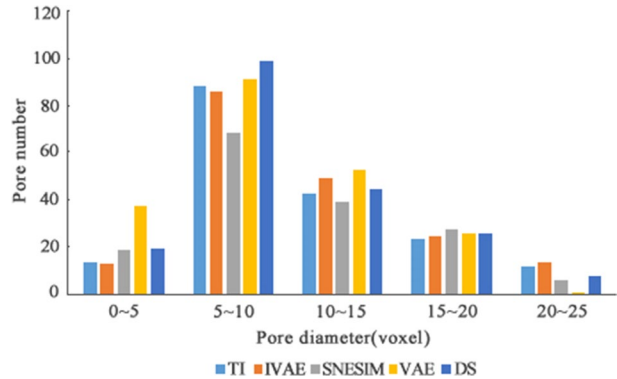
Table 11 The reconstruction time of different layer numbers

| Number of layers (i)	Reconstruction time (s)
4	230
6	350
8	870
10	1420

4.2.7 The Influence of Different $F_{x'}$ and F_z

In this section, we will discuss the influence of different fisher information constraints ($F_{x'}$ and F_z) on the reconstructed results. For convenience, we assume $F_{x'} = F_z$, which are both called "F-constraint" hereafter. Figure 14 shows the MPC curves in three directions for $F_{x'} = F_z = 0.1$, 5 and 10, respectively. It can be seen that with the increase of F-constraint, the reconstruction quality is improved. XOR operation (defined in Sect. 4.2.1) is performed between the TI and each reconstruction, whose results are displayed in Table 12. It seems when F-constraint = 10, overfitting occurs since the XOR result is closer to 0 than the other two situations. Therefore, the F-constraint should be balanced between reconstruction quality and the risk of overfitting. In our experiment, F-constraint equal to 5 is a proper choice.
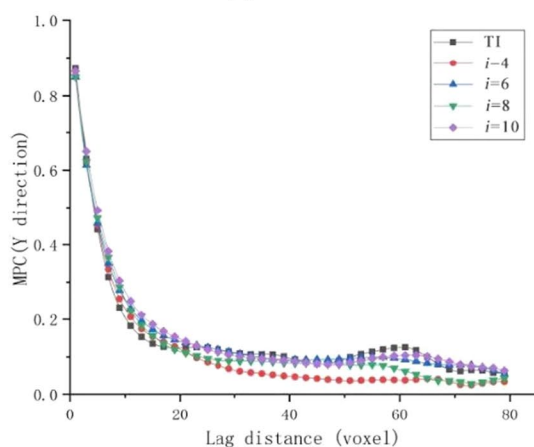
4.2.8 Comparisons of Running Time

Table 13 shows the running time of each method for 10 reconstructions. The reconstruction time in Table 13 consists of the first reconstruction time and the average time of
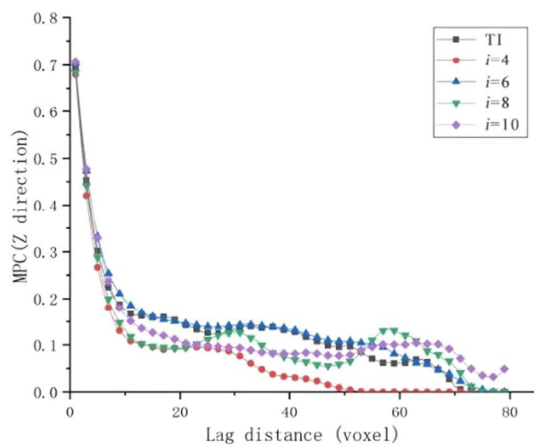
Fig. 13 MPC curves of the TI
and reconstructions using dif-
ferent layer numbers ($i = 4$, 6,
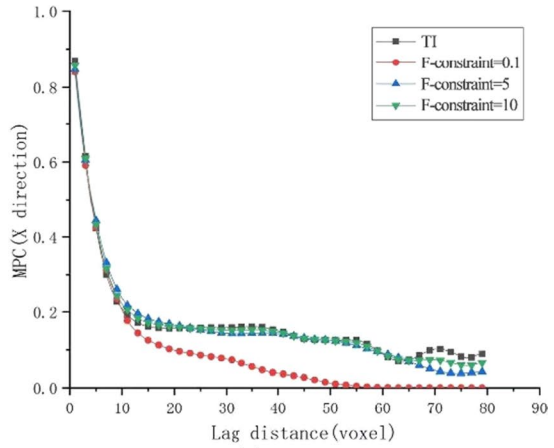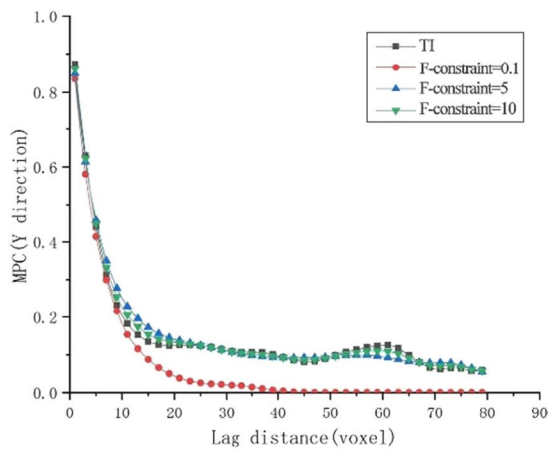8 and 10, respectively) in three
directions
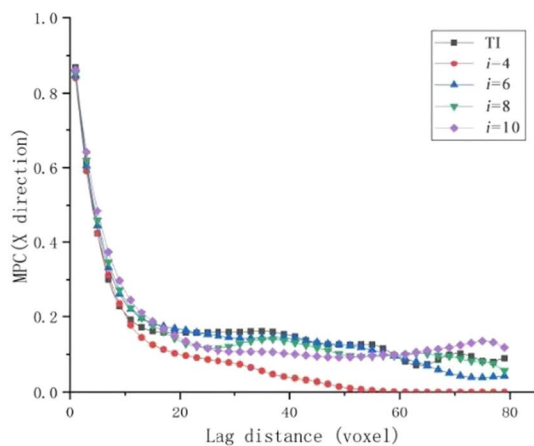
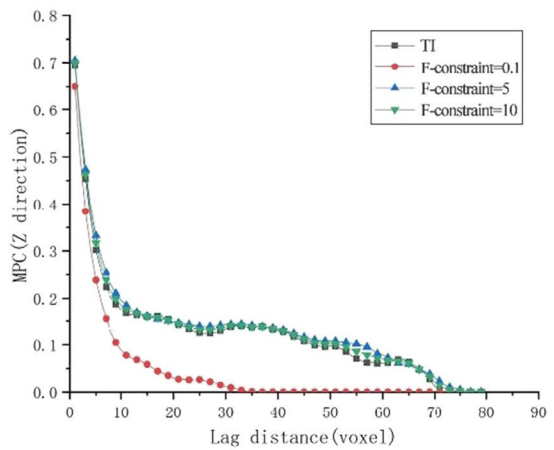**(a)** X direction

(b) Y direction

(c) Z direction

(a) X direction

(b) Y direction

(c) Z direction

Table 12 The XOR results between the TI and each reconstruction

	F-constraint = 0.1 (%)	F-constraint = 5 (%)	F-constraint = 10 (%)
XOR	79.4	26.2	12.7

Table 13 The running time of each method for 10 reconstructions

	SNESIM	VAE	DS	IVAE
First running time (s)	8480	400	22,400	380
The average running time of the remaining 9 reconstructions (s)	8460	350	22,600	350

Table 14 The running times of different reconstruction sizes ($80 \times 80 \times 80$ voxels, $40 \times 40 \times 40$ voxels, $20 \times 20 \times 20$ voxels) for the first running

	$80 \times 80 \times 80$	$40 \times 40 \times 40$	$20 \times 20 \times 20$
First running time (s)	380	62	28

the remaining 9 reconstructions. The reason of splitting the reconstruction time is that the parameters of IVAE and VAE are saved after the first reconstruction, which can be reused in the remaining 9 reconstructions. Hence, IVAE and VAE will use less time after the first reconstruction.

On the contrary, traditional reconstruction methods such as SNESIM and DS have to rescan the training data to establish a new pattern library for each reconstruction because they only store training modes in memory commonly. When a reconstruction process is over, training data in memory will be cleared and therefore, the traditional reconstruction methods need to rescan the TI in each training and cannot reuse the probability information of the first scanning. IVAE model permanently stores the parameters of the training model on the hard disk after the first-round running, so the training model can be directly reused in the reconstruction process in the future, which greatly reduces the total time of multiple reconstructions. Hence, IVAE and VAE shows better efficiency.

To test the different times with different scales, Table 14 displays the running times of different reconstruction sizes ($80 \times 80 \times 80$ voxels, $40 \times 40 \times 40$ voxels, $20 \times 20 \times 20$ voxels) for the first running. It is seen that with the decrease of image scales, the running time also decreases sharply.

5 Conclusions

Traditional numerical methods are widely used in the reconstruction of porous media. However, their applicability has been largely limited because they are normally quite CPU-intensive and need numerous time for reconstruction. These methods usually suffer from the repeatedly scanning of the TI, leading to collecting the statistical information from scratch in every reconstruction. The easy reuse and accurate characterization of statistical

information or reconstruction information surely will promote the reconstruction speed and quality, which possibly can be achieved by bringing deep learning or its variants into the reconstruction of porous media.

In this paper, Fisher information and VAE are combined to reconstruct porous media. The characteristics of the input data are extracted through the encoder; then, the probability distribution of the input data is modeled and the ELBO is redefined according to Fisher information. The proposed model IVAE uses new penalty terms related to Fisher information in the encoder and decoder, respectively, and then calculates the intermediate result using the probability information obtained by the encoder. The final reconstructed porous media have similar structural characteristics with those of the TI. Compared with the traditional numerical methods, our method has shown better efficiency in multiple reconstructions. Compared with VAE, our method has higher reconstruction accuracy.

Declarations

Conflict of interest The authors declare that they have no conflict of interest.

References

Al-Raoush, R., Apostolos, P.: Representative elementary volume analysis of porous media using X-ray computed tomography. Powder Technol. **200**(1–2), 69–77 (2010)

Arns, C.H.: A comparison of pore size distributions derived by NMR and X-ray-CT techniques. Physica A **339**(1–2), 159–165 (2004)

Bakke, S., Øren, P.E.: 3-D pore-scale modelling of sandstones and flow simulations in the pore networks. SPE J. **2**(02), 136–149 (1997)

Bengio, Y., Lamblin, P., Popovici, D., Larochelle, H.: Greedy layer-wise training of deep networks. Proceedings of the 19th international conference on neural information processing system **153–160** (2006)

Blunt, M.J., Bijeljic, B., Dong, H., Gharbi, O., Iglauer, S., Mostaghimi, P., Paluszny, A., Pentland, C.: Pore-scale imaging and modelling. Adv. Water Resour. **51**, 197–216 (2013)

Burda, Y., Grosse, R., Salakhutdinov, R.: Importance weighted autoencoders. arXiv: 1509.00519 (2015)

Chen, X., Kingma, D.P., Salimans, T., Duan, Y., Dhariwal, P., Schulman, J., Sutskever, I., Abbeel, P.: Variational lossy autoencoder. International conference on learning representation (2016)

Cormen, T.H., Leiserson, C.E., Rivest, R.L., Stein, C.: Introduction to algorithms. MIT Press (2009)

Costanza, Robinson, M.S., Estabrook, B.D., Fouhey, D.F.: Representative elementary volume estimation for porosity, moisture saturation, and air water interfacial areas in unsaturated porous media: Data quality implications. Water Resour. Res. **47**(7), 07513.1–07513.12 (2011)

Dembo, A., Cover, T.M., Thomas, J.A.: Information theoretic inequalities. IEEE Trans. Inf. Theory **37**(6), 1501–1518 (1991)

Fisher, R.A.: On the mathematical foundations of theoretical statistics. Philos. Trans. R. Soc. Lond. Ser. A **222**, 309 (1922).

Fisher, R.A.: Theory of statistical estimation. Proc. Cambridge Philos. Soc. **22**, 700–725 (1925)

Frieden, B.R.: Science from Fisher information: A Unification. Cambridge University Press (2004).

Hemes, S., Desbois, G., Urai, J.L., Desbois, G., Urai, J.L., Schröppel, B., Schwarz, J.O.: Multi-scale characterization of porosity in Boom Clay (HADES-level, Mol, Belgium) using a combination of X-ray μ-CT, 2D BIB-SEM and FIB-SEM tomography. Microporous Mesoporous Mater. **208**, 1–20 (2015)

Hidajat, I., Rastogi, A., Singh, M., Mohanty, K.K.: Transport properties of porous media from thin-sections. SPE J. **7**(1), 40–48 (2002)

Hinton, G.E., Osindero, S., Teh, Y.W.: A fast learning algorithm for deep belief nets. Neural Comput. **18**(7), 1527–1554 (2006)

Ioannidis, M.A., Kwiecien, M., Chatzis, I.: Computer generation and application of 3d model porous media: from pore-level geostatistics to the estimation of formation factor. Petroleum computer conference (1995)

James, M.J.: Kullback-leibler divergence. International Encyclopedia of Statistical Science **720–722** (2011)

Karsanina, M.V., Gerke, K.M., Skvortsova, E.B., Mallants, D.: Universal spatial correlation functions for describing and reconstructing soil microstructure. Plos One **10**(5), e0126515 (2015)

Kingma, D.P., Welling, M.: Auto-encoding variational bayes. International conference on learning representations **14–27** (2014)

Louizos, C., Swersky, K., Li, Y., Welling, M., Zemel, R.: The variational fair autoencoder. arXiv: 1511.00830 (2015)

Mahmud, K., Mariethoz, G., Caers, J., Tahmasebi, P., Baker, A.: Simulation of Earth textures by conditional image quilting. Water Resour. Res. **50**, 3088–3107 (2014)

Makhzani, A., Shlens, J., Jaitly, N., Goodfellow, L., Frey, B.: Adversarial autoencoders. arXiv: 1511.05644 (2015)

Nash, C., Williams, C.K.I.: The shape variational autoencoder: a deep generative model of part-segmented 3D objects. Computer Graphics Forum **36**(5), 1–12 (2017)

Nordahl, K., Ringrose, P.S.: Identifying the representative elementary volume for permeability in heterolithic deposits using numerical rock models. Math. Geosci. **40**(7), 753–771 (2008)

Oda, M.: A method for evaluating the representative elementary volume based on joint survey of rock masses. Can. Geotech. J. **25**(3), 440–447 (1988)

Okabe, H., Blunt, M.J.: Pore space reconstruction using multiple-point statistics. J. Petrol. Sci. Eng. **46**(1–2), 121–137 (2005)

Okabe, H., Blunt, M.J.: Prediction of permeability for porous media reconstructed using multiple-point statistics. Phys. Rev. E **70**(6), 066135 (2004)

Øren, P.E., Bakke, S.: Process based reconstruction of sandstones and prediction of transport properties. Transp. Porous Media **46**(2–3), 311–343 (2002)

Phuong, M., Welling, M., Kushman, N., Tomioka, R., Nowozin S.: The mutual autoencoder: Controlling information in latent code representations. ICLR 2018 conference blind submission (2018)

Quiblier, J.A.: A new three-dimensional modeling technique for studying porous media. Colloid Interface Sci. **98**, 84–102 (1984)

Rezende, D.J., Mohamed, S.: Variational inference with normalizing flows. Comput. Sci. **34**(6), 421–427 (2015)

Rosso, O.A., Olivares, F., Plastino, A.: Noise versus chaos in a causal fisher-shannon plane. Papers Phys. **7**, 070006 (2015)

Rumelhart, D.E., Hinton, G.E., Williams, R.J.: Learning representations by back-propagating errors. Nature **323**(6088), 533–536 (1986)

Samuel, R.B., Luke, V., Oriol, V., Andrew, M.D., Samy, B.: Generating sentences from a continuous space. arxiv:1511.06349 (2015)

Schrödinger, E.: About heisenberg uncertainty relation. Proc. Prussian Acad. Sci. Phys. Math. XIX. **293** (1930)

Shannon, C., Weaver, W.: The mathematical theory of communication. University of Illinois Press (1949)

Stam, A.J.: Some inequalities satisfied by the quantities of information of fisher and shannon. Inf. Control **2**(2), 101–112 (1959)

Strebelle, S.: Conditional simulation of complex geological structures using multiple-point statistics. Math. Geol. **34**(1), 1–21 (2002)

Stingaciu, L.R., Weihermuller, L., Haberpohlmeier, S.: Determination of pore size distribution and hydraulic properties using nuclear magnetic resonance relaxometry: a comparative study of laboratory methods. Water Resour. Res. **46**(11), 2387–2392 (2010)

Tahmasebi, P., Hezarkhani, A., Sahimi, M.: Multiple-point geostatistical modeling based on the cross-correlation functions. Comput. Geosci. **16**(3), 779–797 (2012)

Tahmasebi, P., Sahimi, M.: Reconstruction of three-dimensional porous media using a single thin section. Phys. Rev. E Stat. Nonlin. Soft Matter Phys. **85**(6), 066709 (2012)

Tomutsa, L., Silin, D., Radmilovic, V.: Analysis of chalk petrophysical properties by means of submicron-scale pore imaging and modeling. SPE Reservoir Eval. Eng. **10**(3), 285–293 (2007)

Vignat, C., Bercher, J.F.: Analysis of signals in the Fisher-Shannon information plane. Phys. Lett. A **312**(1–2), 27–33 (2003)

Vincent, P., Larochelle, H., Bengio, Y., Manzagol P.A.: Extracting and composing robust features with denoising autoencoders. Proceedings of the 25th international conference on machine learning **1096–1103** (2008)

Wirth, R.: Focused Ion Beam (FIB): A novel technology for advanced application of micro- and nanoanalysis in geosciences and applied mineralogy. Eur. J. Mineral. **16**(6), 863–876 (2004)

Wirth, R.: Focused Ion Beam (FIB) combined with SEM and TEM: advanced analytical tools for studies of chemical composition, microstructure and crystal structure in geomaterials on a nanometre scale. Chem. Geol. **261**(3–4), 217–229 (2009)

Zhang, T., Du, Y., Huang, T., Yang, J., Lu, F., Li, X.: Reconstruction of porous media using ISOMAP-based MPS. Stoch. Env. Res. Risk Assess. **30**(1), 395–412 (2016)

Zhang, T., Switzer, P., Journel, A.: Filter-based classification of training image patterns for spatial simulation. Math. Geol. **38**(1), 63–80 (2006)

Zhao, S., Song, J., Ermon, S.: InfoVAE: Information maximizing variational autoencoders. arxiv:1706.02262 (2017)

Zheng, H., Yao, J., Zhang, Y., Tsang, I.W. and Wang, J.: Understanding vaes in fisher-shannon plane. In Proceedings of the AAAI conference on artificial intelligence **33**(1), 5917–5924 (2019).